Journal of Advanced Ceramics https://mc03.manuscriptcentral.com/jacer
https://doi.org/10.26599/JAC.2024.9220894

Research Article

The study of grain growth behavior and properties of high-entropy pseudobrookite $(Mg,Co,Ni,Zn)Ti_2O_5$ ceramics

Xiaohui Ma[a], Jinyu Wu[a], Lingyi Meng[b], Jinfeng Zhang[a], Heng Chen[b], Liwen Yan[a], Anran Guo[a]*, Jiachen Liu[a]*

[a]*School of Materials Science and Engineering, Key Laboratory of Advanced Ceramics and Machining Technology of Ministry of Education, Tianjin University, Tianjin 300072, China*

[b]*Xiamen Key Laboratory of Rare Earth Photoelectric Functional Materials, Xiamen Institute of Rare Earth Materials, Haixi Institutes, Chinese Academy of Sciences, Xiamen 361021, China*

* Corresponding author.

E-mail: jcliutju@tju.edu.cn

E-mail: arguo@tju.edu.cn

Received: January 24, 2024; Revised: April 8, 2024; Accepted: April 8, 2024

Abstract: It is well known that the grain size of high-entropy ceramics is quite small owing to the so-called sluggish diffusion effect. However, the abnormal grain growth behavior often occurs in high-entropy pseudobrookite ceramics, finally resulting in the formation of many abnormally grown grains with the grain size as large as 50 μm. To study this phenomenon, the grain growth behavior of high-

entropy pseudobrookite ceramics is systematically investigated in this paper. The results demonstrate that the starting material powders firstly react with each other to form a high-entropy intermediate phase and calcined TiO_2 powders (TiO_2-1100 ℃), and then as the sintering temperature increases, the formed high-entropy intermediate phase further react with TiO_2-1100 ℃ to form high-entropy pseudobrookite ceramics. Thus, in this system, besides the sluggish diffusion effect, the grain sizes of the high-entropy intermediate phase and TiO_2-1100 ℃ also affect the morphology of high-entropy pseudobrookite. Compared to nano-sized TiO_2, micron-sized TiO_2 has lower sintering activity. Therefore, the high-entropy intermediate phase (Mg,Co,Ni,Zn)TiO_3 and TiO_2-1100 ℃ prepared with micron-sized starting materials exhibits lower grain sizes, finally resulting in the formation of high-entropy (Mg,Co,Ni,Zn)Ti_2O_5 with small grain size. What's more, nano-indentation and thermal conductivity tests are carried out on high-entropy (Mg,Co,Ni,Zn)Ti_2O_5 with different morphologies. The results show that the hardness of high-entropy (Mg,Co,Ni,Zn)Ti_2O_5 increases from 6.05 GPa to9.95 GPa as the grain size refinement, whereas thermal conductivity decreases from 2.091±0.006 $Wm^{-1}K^{-1}$ to 1.583±0.006 $Wm^{-1}K^{-1}$. All these results indicate that high-entropy (Mg,Co,Ni,Zn)Ti_2O_5 with small grain size is a potential material for thermal protection.

Keywords: grain size; sluggish diffusion effect; two-step solid phase process; high-entropy intermediate phase; high-entropy pseudobrookite ceramic

1 Introduction

High entropy materials is an emerging class of multicomponent solid solution materials, which is proposed in the field of alloys firstly in 2004. Following that, this concept is used in high entropy ceramics (HECs) [1,2]. Compared with the traditional ceramics, HECs possess many interesting properties owing to its four core effects, such as stable phase structure, high corrosion, oxidation

resistance, and unique mechanical properties, making them ideal materials for a wide range of applications [3-5].

Sintering is a high temperature process for consolidating ceramic powders during which both densification and grain growth occurred. A few grains can grow at a very fast rate under certain conditions, which is known as abnormal grain growth (AGG). In the production process of polycrystalline materials, AGG may lead to a heterogeneous grain morphology, which is typically harmful to material performance, particularly mechanical properties. Therefore, controlling grain growth behavior during sintering is a very important topic to obtain high-performance ceramic materials. According to the studies, the grain growth in high-entropy ceramics at high temperatures is relatively slower than that in the corresponding single-component ceramics owing to the sluggish diffusion effect. Inspired by it, Zhou et al. [6,7] successfully prepared high-entropy (TiZrNbTaMo)C and $(La_{0.2}Ce_{0.2}Nd_{0.2}Sm_{0.2}Eu_{0.2})_2Zr_2O_7$ with fine grains. Then Su et al. [8] used polyacrylamide gel technology to successfully solve the problems of grain coarsening and particle aggregation of high-entropy ceramics during sintering. By using a plasma-assisted ball milling technique, Wang et al. [9] enhance the sintering characteristics and prepare high-entropy fluorite oxide ceramics with little AGG and good density and mechanical qualities. However, studies of Zhang et al. [10] have shown that the sluggish diffusion effect does not dominate the grain growth behavior of high-entropy ceramics owing to the defects formed during the synthesis process, and resulting in a rapid grain growth of high-entropy ceramics at high temperatures. Thus, studying the growing process of high-entropy ceramics grains is an attractive scientific topic.

The pseudobrookite ceramics are used as high-temperature insulation materials, water purification filters, and diesel particulate filters owing to their low thermal conductivity, high melting point, low coefficient of thermal expansion, and excellent thermal shock tolerance [11-13]. Nevertheless, the structure of pseudobrookite is unstable and prone to disintegration, which severely limits its future application below 1200 ℃ [14,15]. To solve the above-mentioned problems, Wu et al. [16] proposed

that the properties of the pseudobrookite ceramics can be enhanced by forming high-entropy phases. Mg, Co, Ni, and Zn were selected for the M position in high-entropy pseudobrookite phase, as these metal elements have been proved to have good compatibility and high doping amounts in the lattice of pseudobrookite phase. However, the phenomenon of AGG is still found during the preparation of high-entropy $(Mg,Co,Ni,Zn)Ti_2O_5$ which is characterized by the coexistence of equiaxed grains and rod-like grains. As is well known, this type of AGG will undoubtedly have a negative impact on its performance. To solve these problems, an in-depth study of grain growth behavior of high-entropy pseudobrookite should be carried out.

Currently, typical high-entropy ceramics are generated in a single step. However, it shows that high-entropy pseudobrookite ceramics are formed through a two-step solid phase process. Therefore, in addition to the sluggish diffusion effect slowing the grain growth, the grain sizes of high-entropy intermediate phase and calcined TiO_2 also affect the occurrence of AGG in the high-entropy pseudobrookite ceramics. To support this finding, three $(Mg,Co,Ni,Zn)Ti_2O_5$ are successfully prepared by three different starting material powders with varying size distributions. The research results indicate that the high-entropy $(Mg,Co,Ni,Zn)Ti_2O_5$ prepared by micron-sized starting materials has a small grain size and exhibit excellent hardness and thermal conductivity.

2 Experimental procedure

The high-entropy pseudobrookite $(Mg,Co,Ni,Zn)Ti_2O_5$ (MT2).and $CoTi_2O_5$ were prepared through the in-situ solid-phase reaction method using the corresponding individual metallic oxides as the starting materials. In this study, Mg, Co, Ni, and Zn were selected for the M position in MT2. Micron-sized CoO and rutile were used to prepare $CoTi_2O_5$; Three different particle size starting material components were selected to synthesize MT2. Component 1 was composed of four micron-sized metallic oxides (μM) and micron-sized rutile (μT2), and the high-entropy $(Mg,Co,Ni,Zn)Ti_2O_5$ prepared by component 1 was called as μMμT2; Component 2 was composed of four micron-sized metallic oxides (μM) and nano-sized rutile(nT2) and the high-entropy $(Mg,Co,Ni,Zn)Ti_2O_5$ prepared

by component 2 was called as μMnT2; Component 3 was composed of four nano -sized metallic oxides (nM) and nano-sized rutile (nT2) and the high-entropy (Mg,Co,Ni,Zn)Ti_2O_5 prepared by component 3 was called as nMnT2.

MgO (99%, 3 μm), MgO (99.9%, 50 nm), ZnO (99.9%, 3 μm), ZnO (99.5%, 30 nm), TiO_2 (rutile, 99%, 2-3 μm) and TiO_2 (rutile, 99.5%, 40 nm) were purchased from Macklin Biochemical Co., Ltd., Shanghai, China; CoO (99.9%, 2 μm), Co_3O_4 (99.5%, 30 nm), NiO (99%, 4 μm) and NiO (99.5%, 30 nm) were purchased from Aladdin Biochemical Technology Co., Ltd., Shanghai, China. The particle sizes of starting materials are shown in Fig. 1. The average particle sizes of micron-sized raw materials are between 2-5 μm. Whereas, the average particle sizes of nano-sized raw materials are between 30-50 nm. All reagents were used as received. All the oxide powders were weighed by stoichiometry (to ensure that the molar ratio of the sum of metallic oxides to titanium dioxide was 1:8), and mixed by ball-milled at 200 r/min for 10 h with ethanol as the dispersing phase. After drying and sieving, powder mixtures were added with Polyvinyl alcohol (PVA) and then press into pellets. The powder compacts were pressed under 40 MPa for 10min and then sintered at 1400 ℃ for 2 h in air to prepare the ceramic specimens.

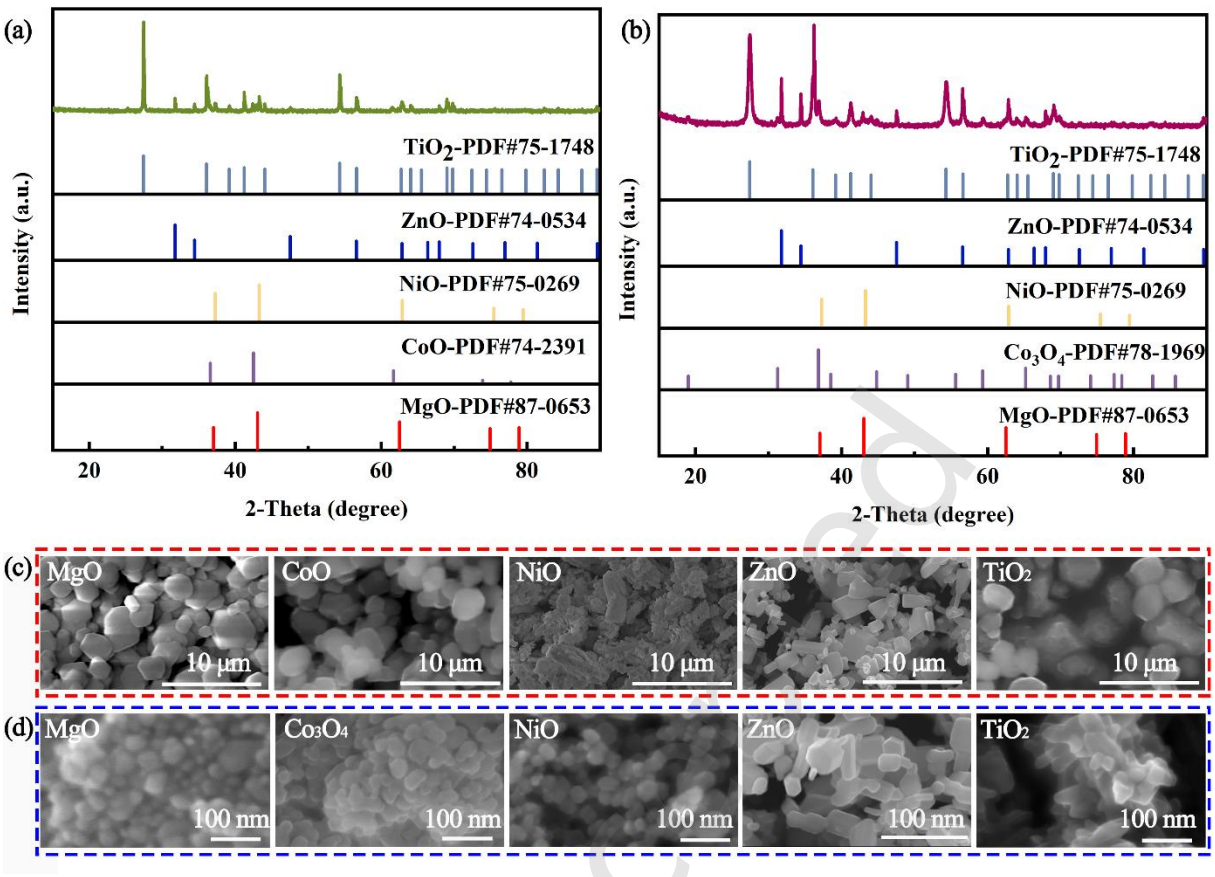

Fig.1 The XRD pattern of (a) micron-sized raw particles and (b) nano-sized raw particles and the SEM image of (c) micron-sized raw particles and d) nano-sized raw particles.

The phase composition of as-synthesized powders was identified by X-ray diffraction (Bruker, D8 Advanced, Germany) using Cu Kα radiation (λ = 1.5406 Å) with a step size of 0.02° at a scanning rate of 2 °/min. The high-resolution microstructure, crystal structure and the element distributions of high-entropy MT_2 specimens were studied by the transmission electron microscope (JEOL, Jem-F200, Japan) and energy disperse spectrometer (Oxford, X-Max20, UK), respectively. The chemical states and chemical environment of the metallic elements in high-entropy MT2 were analyzed by the X-ray photoelectron spectrometer (Kratos, Axis supra, UK) with Al K_α X-ray source. All data were calibrated to the adventitious C 1s peak at 284.8 eV. The surfaces of samples are used for SEM automatically observation after sintering at designated temperatures. The scanning electron microscope (Zeiss, Sigma 300, Germany) was used to characterize the microstructures. The EBSD samples were polished by 1061 SEM mill at 8 Kv for 45 min and 4 Kv for 30 min. The value of the average area and the

number of grain boundary of MT2s are obtained by the analysis of EBSD. The EBSD measurements were performed on a JSM-7800F scanning electron microscope in an area of 400 × 350 μm^2. Nano-indentation testing (Hysitron TI-Premier Corp, Hysitron TI-Premier, USA) was performed with a Berkovich pyramid shaped diamond tip to determine the elastic modulus and hardness. The test applied a maximum load of 5 mN on samples within 15 s and held for 2 s at peak load. The thermal conductivity was obtained by the transient plane source (TPS) method (Hot Disk, Tps2500s, Sweden). The reaction temperature was obtained by differential scanning calorimeter (NETZSCH, Bavaria, Germany) in heat flux DSC mode. The samples (60 mg) were heated in platinum crucibles at a rate 10 ℃ min^{-1} in air atmosphere from room temperature to 1400 ℃.

3 Results and discussion

3. 1 Phases and microstructures of the as-sintered ceramics

The XRD and SEM analyses of high-entropy μMμT2, μMnT2 and nMnT2 are displayed in Fig. 2. As shown in XRD pattern (Fig. 2(a)), the existence of harp peaks suggests that a well-crystallized structure is formed in all the three samples. Pseudobrookite structure ($CoTi_2O_5$, JCPDS Card No. 76-1600, *Cmcm*, a = 3.732 Å, b = 9.718 Å, c = 10.069 Å) can be clearly detected in these three samples without the formation of any second phase or mesophase. Fig. 2(b)-2(c) show the high-resolution TEM (HRTEM) images and the corresponding selected area electron diffraction (SAED) patterns of high-entropy μMμT2. In Fig. 2(b), the lattice fringes with an interplanar distance of 0.340 nm are obtained by measuring the average distance of 11 parallel fringes, which corresponds to the d-spacing of $(\bar{1}\bar{1}0)$ plane in pseudobrookite structure. Furthermore, the related SAED pattern along the $[1\bar{1}0]$ direction displayed in Fig. 2(c) also confirms that the crystal structure of synthesized μMμT2 belongs to pseudobrookite phase. Fig. 2(e) and Fig. 2(h) show HRTEM images taken along the $[3\bar{3}4]$ and $[\bar{3}3\bar{2}]$ axis, respectively. A lattice stripe distance of around 0.34 nm is found in both images, which corresponds to the interplanar distance of the {110} face in pseudobrookite. Moreover, the element

distribution in samples is analyzed by the energy dispersive spectroscopy (EDS) in STEM. The EDS maps in Fig. 2(d), 2(g) and 2(j) show that the elements Mg, Co, Ni, Zn, Ti and O are uniformly distributed at the micro-level in three MT2s without significant chemical clustering or elemental segregation. As consequence, the results of XRD analyses, together with TEM and STEM-EDS analyses, strongly support that the synthesized μMμT2, μMnT2 and nMnT2 are all pseudobrookite-structured and show a great chemical uniformity.

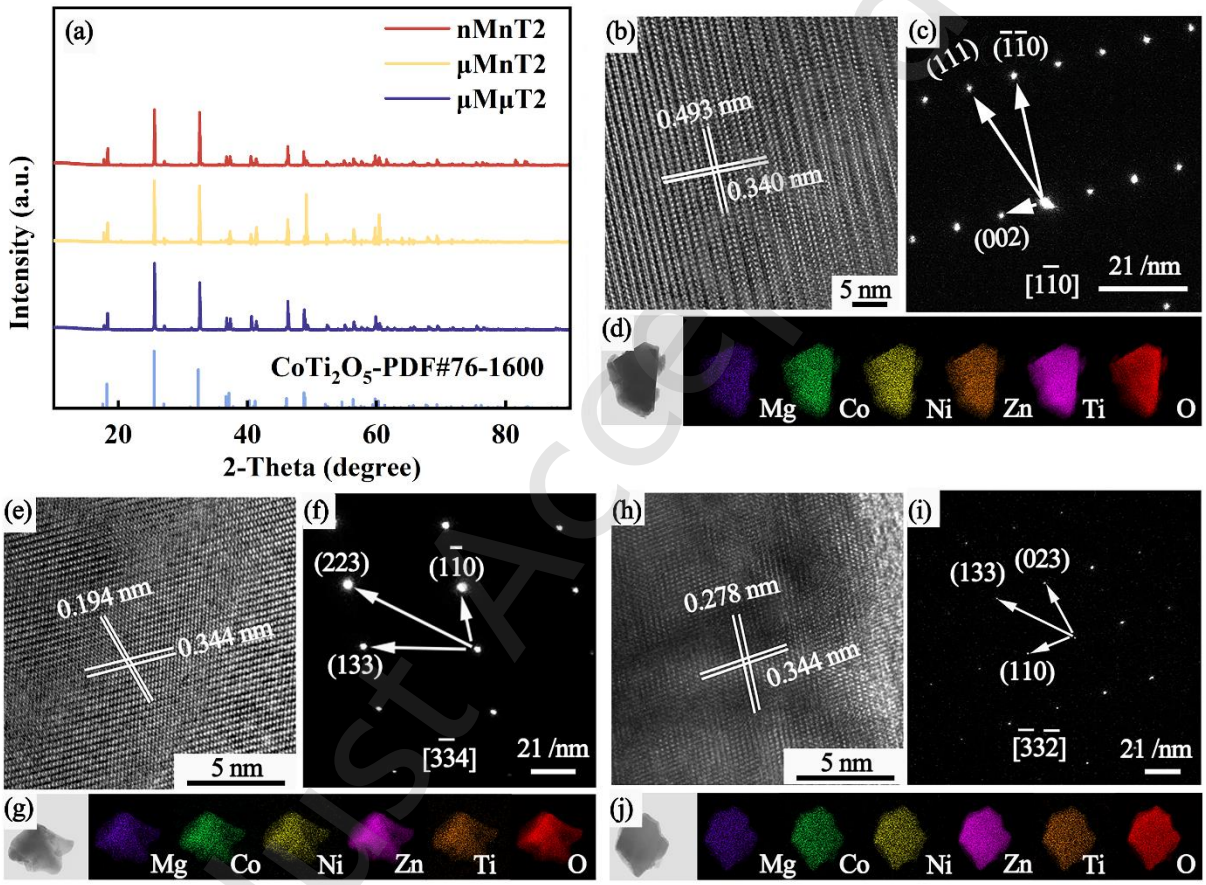

Fig.2 (a) XRD pattern of MT2s; Enlarged HAADF STEM, corresponding SAED pattern and Elemental mapping of (b)–(d) μMμT2, (e)–(g) μMnT2, (h)–(j) nMnT2.

3. 2 Structure analysis of high-entropy (Mg,Co,Ni,Zn)Ti_2O_5

Fig. 3 shows the total spectrums and core energy level spectrums of the corresponding elements obtained by XPS. Each of the constituent elements in the three MT2s, including Mg, Co, Ni, Zn, Ti, and O, are visible in the resulting XPS data, which is consistent with the elemental mapping results of

the EDS in Fig. 2. Fig. 3(a) shows the XPS spectra of Mg 1s, Co 2p. Ni 2p. Zn 2p and Ti 2p in μMμT2. The binding energy of Mg 1s in high-entropy (Mg,Co,Ni,Zn)Ti_2O_5 is ~1303.14 eV, which is consistent with the binding energy of Mg^{2+} in $MgTi_2O_5$ [17]. Similarly, the Co 2p spectrum shows four peaks at ~795.57 eV and ~780.06 eV with satellite peaks at ~803.00 eV and ~786.95 eV, which are almost comparable to the binding energy and peak shape of Co^{2+} in $CoTi_2O_5$ [18]. For the Ni ions in high-entropy (Mg,Co,Ni,Zn)Ti_2O_5, the binding energies of Ni 2p1/2 and 2p3/2 are ~872.73 and ~855.19 eV, respectively, which are similar with the binding energies of the Ni^{2+} in typical Ni insulators [19,20]. Furthermore, the strong satellite peaks at ~861.65 and ~879.79 eV correspond to the satellite structure of high-spin Ni^{2+} in octahedral position [18]. As to the Zn ions in high-entropy (Mg,Co,Ni,Zn)Ti_2O_5, the binding energies of Zn 2p3/2 and Zn 2p1/2 are ~1021.27 and ~1044.22 eV, respectively, which are consistent with the binding energies of typical Zn^{2+} [21,22]. The two detected peaks of Ti 2p spectrum are located at ~458.51 eV and 464.40 eV which can be attributed to Ti 2p3/2 and Ti 2p1/2. Further investigation reveals that the Ti species are only present in the form of Ti^{4+} rather than Ti^{3+} in obtained samples. Additionally, the binding energies of the constituent elements of Fig. 3(b) (μMnT2) and Fig. 3(c) (nMnT2) are nearly equal to those of Fig. 3(a) (μMμT2). In conclusion, the XPS results indicate that the chemical states and chemical environments of Mg, Co, Ni, Zn, and Ti ions in three MT2s are identical.

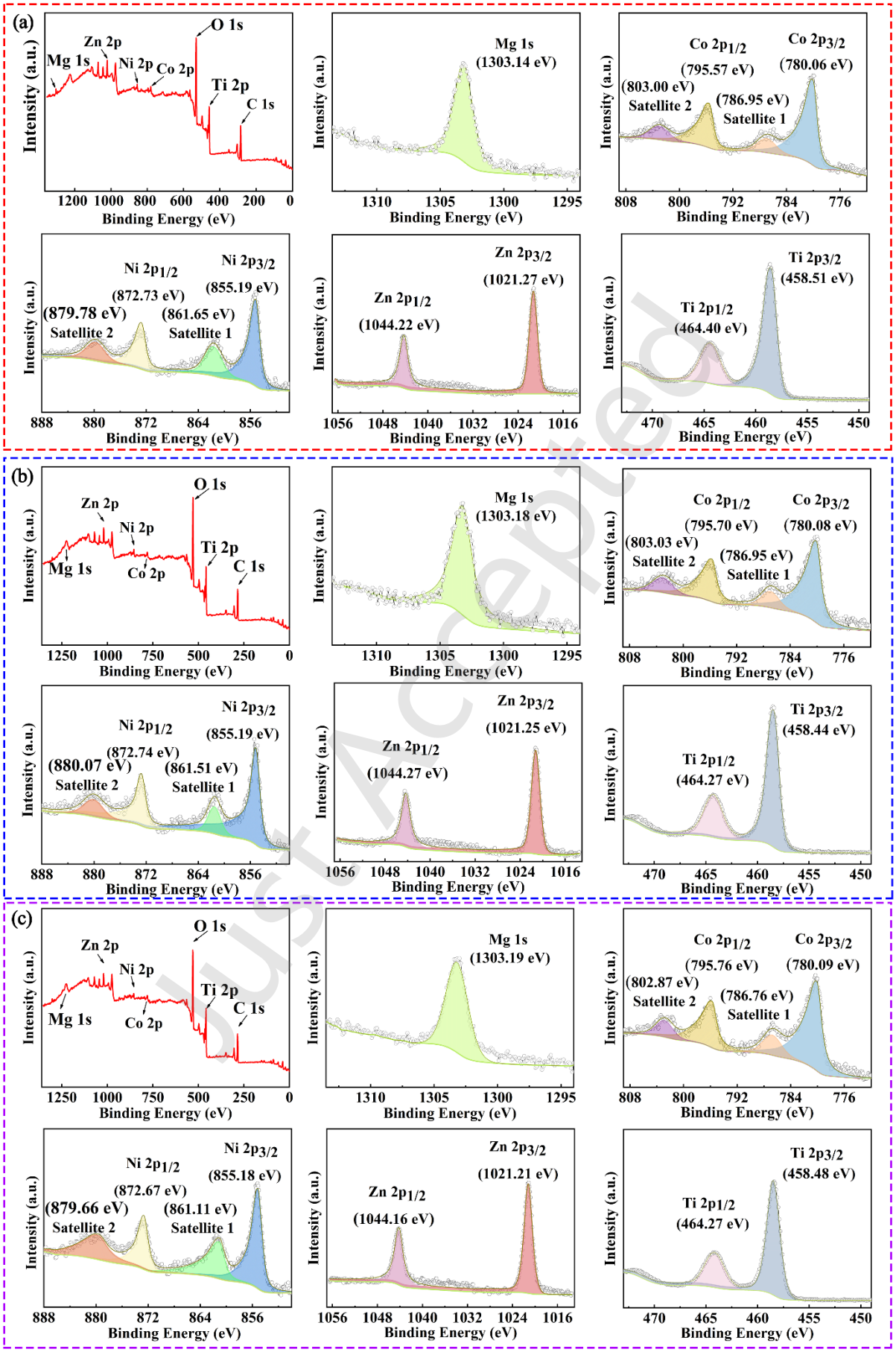

Fig. 3 XPS spectra of survey spectra, Mg 1s, Co 2p, Ni 2p, Zn 2p, and Ti 2p of (a) μMμT2, (b) μMnT2 and (c) nMnT2.

3. 3 Analysis of grain growth habit in pseudobrookite ceramic

Fig. 4 displays the microstructure of three MT2s and $CoTi_2O_5$. Three different particle sizes of **starting** materials (component 1 to component 3) are sintered at 1400 ℃ for 2h to form three MT2. $CoTi_2O_5$ is formed by micron-sized CoO and TiO_2 reacted with each other at 1400 ℃ for 2h. It shows that the grain size of all MT2s is much smaller than that of its single-phase $CoTi_2O_5$ (shown in Fig. 4(d)). This is because the sluggish diffusion effect decreases the thermodynamic driving force for grain growth at high temperature and avoids the grain coarsening [23,24]. According to Fig. 4(a), μMμT2 has a large number of uniformly equiaxed crystals. The grain size of μMμT2 ranges 3 to 21 μm with an average of 6.52 μm. In contrast, Fig. 4(b)-4(c) indicate that the μMnT2 and nMnT2 grains both exhibit typical morphology of pseudobrookite phase (coexistence of rod-like and equiaxed grains). The appearance of rod-like grains leads to an increase in average grain size and decrease in grain size uniformity of high-entropy pseudobrookite ceramics. The average grain size of μMnT2 is 9.34 μm which is somewhat slightly larger than that of μMμT2 and the length of the rod-like particles is as large as 39.53 μm. Notably, the average grain size of nMnT2 rises to 13.48 μm and the length of plate-like particles reaches to 100 μm, which is obviously larger than that of μMμT2 and μMnT2. This indicates that the sluggish diffusion effect is not the only key factor controlling the grain growth of high-entropy pseudobrookite ceramics, the grain size of high-entropy pseudobrookite ceramics increases as the starting material particle size decreases under the same sintering process.

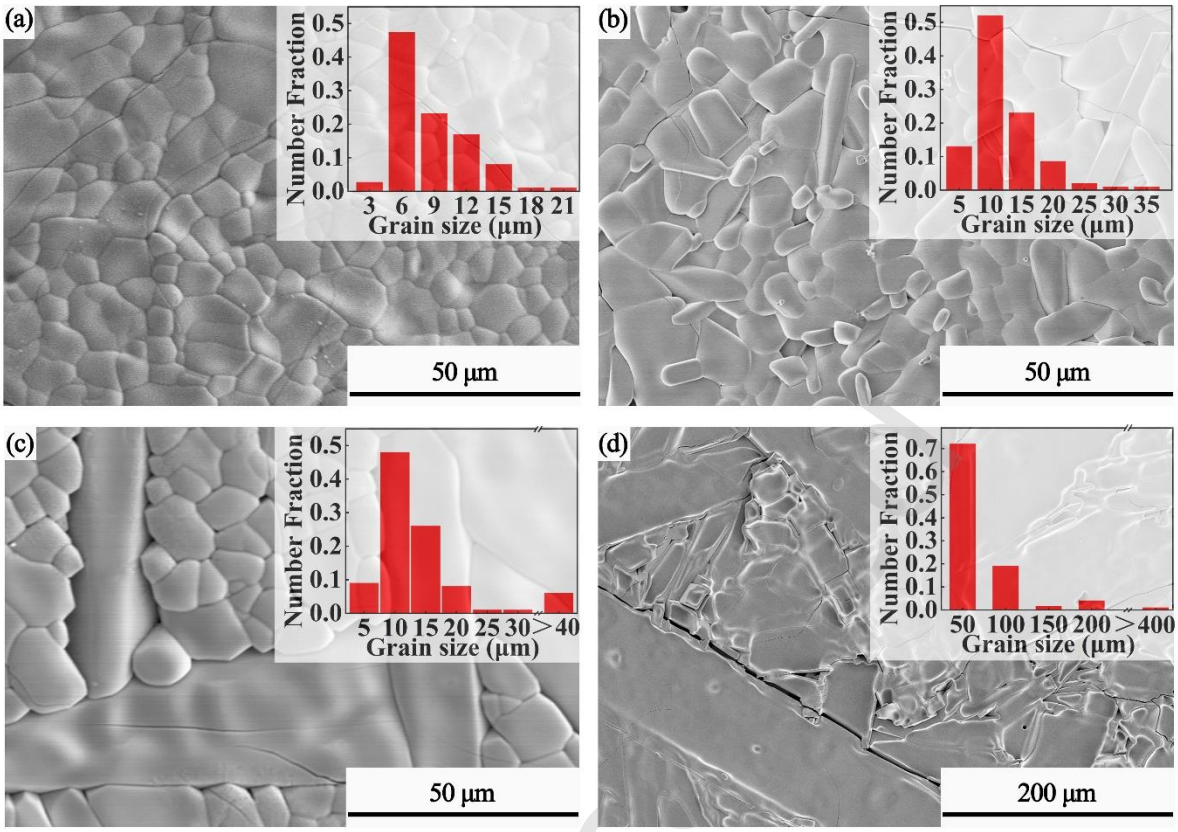

Fig. 4 SEM image of (a) μMμT2, (b) μMnT2, (c) nMnT2 and (d) $CoTi_2O_5$ synthesized at 1400 ℃.

The rod-like particles are discovered to be the typical morphology of pseudobrookite ceramics which are caused by the AGG at high temperatures [25]. EBSD is used to characterize grain orientation in ceramics to further examine the abnormal growth of the grains. IPF maps of MT2 ceramics synthesized from three components are shown in Fig. 5(a)-5(c), where different colors represent different relative crystal orientations, and closer colors reflect closer grain orientations. Generally, grain boundaries with the misorientation angle higher than 15° are called as large angle grain boundary and grain boundaries with the misorientation angle less than 15° are called as low angle grain boundary, as represented by black and white lines in Fig. 5(a)-5(c), respectively. In μMμT2, there are many large pseudobrookite domains that are subdivided into very small-sized subgrains with very similar orientations. This is evidenced by the very similar subgrains colors within a pseudobrookite domain in Fig. 5(a). Compared to the μMμT2, the grain size of μMnT2 has significantly increased. As a result of grain size coarsening, the number of low-angle boundaries decreases from 35.6% to 22.8%, while the number of high-angle

boundaries increases from 64.4° to 77.2°, as shown in Fig. 5(d). In the case of nMnT2 (as illustrated in Fig. 5(c)), the particles studied appear to be made up of pseudobrookite grains with nearly no subdivisions. Furthermore, nMnT2 contains a significant percentage of high-angle boundaries (the majority misorientation angles are between 80° and 100°). As is known that the grain boundary energy of large-angle boundaries is much higher than that of low-angle boundaries, and resulting in a quicker migration of grain boundaries which promotes grain growth. Thus, the grain growth rate of μMnT2 and nMnT2 are faster than that of μMμT2 in this study.

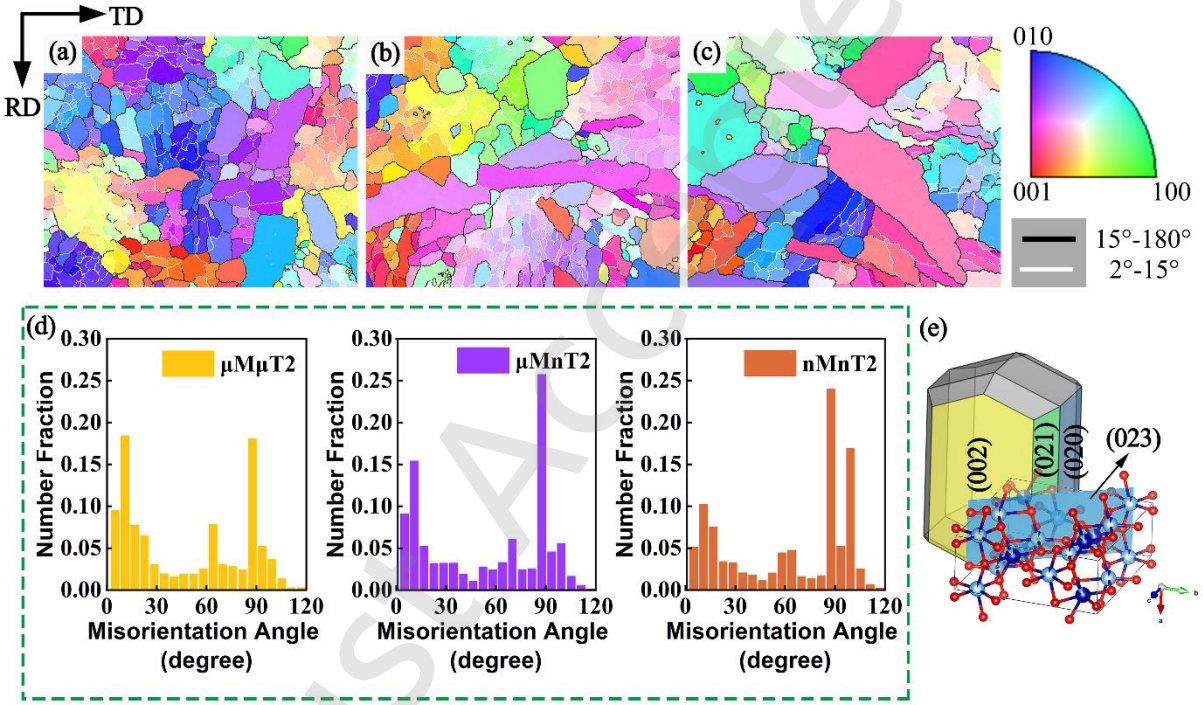

Fig. 5 IPF maps of (a) μMμT2, (b) μMnT2 and (c) nMnT2; (d) misorientation angle of MT2s; (e) the morphology predictions of pseudobrookite phase.

It is noteworthy that the crystal orientations of rod crystal plane in μMnT2 and nMnT2 are basically the same. As shown in Fig. 5(b)-5(c), the length of (010) and (001) planes are longer than that of (100) plane. To further comprehend this phenomenon, DFT and BFDH techniques are utilized to analyze the growth of each crystal plane. The crystal structure, as is well known, determines the growth behavior of grains. And the previously mentioned investigations support that the single-phase $CoTi_2O_5$ and

high-entropy (Mg,Co,Ni,Zn)Ti_2O_5 are pseudobrookite phases. Therefore, $CoTi_2O_5$ is used in this study to calculate the theoretical growth habit of high-entropy (Mg,Co,Ni,Zn)Ti_2O_5.

The $CoTi_2O_5$ cells are cut along the (100), (010), and (001) planes, and the vacuum slab thickness is set as 15 Å. A 2 × 2 supercell is created perpendicular to the z-axis and the models are shown in Fig. 6. The Equation 1 is then used to calculate the surface energy of the low-index surfaces (100), (010), and (001) planes, which are determined to be 8.36, 6.47, and 5.49 eV/nm^2, respectively. According to the calculated results, the (100) plane has a higher surface energy than the (010) and (001) planes, which causes the cell grow significantly along the vertical direction of (100) plane. Because of the difference in grain growth rate of different crystal faces, the slower growing (010) and (001) planes extend along the a-axis during grain growth and are finally kept according to the Bravais rule.

$$\gamma = \frac{A}{2} \times (E_{slab} - E_{bulk}) \quad (1)$$

Where E_{slab} is the energy of the model, E_{bulk} is the energy of an equal number of formula units in the bulk and A is the surface area of one face in the slab model [26,27].

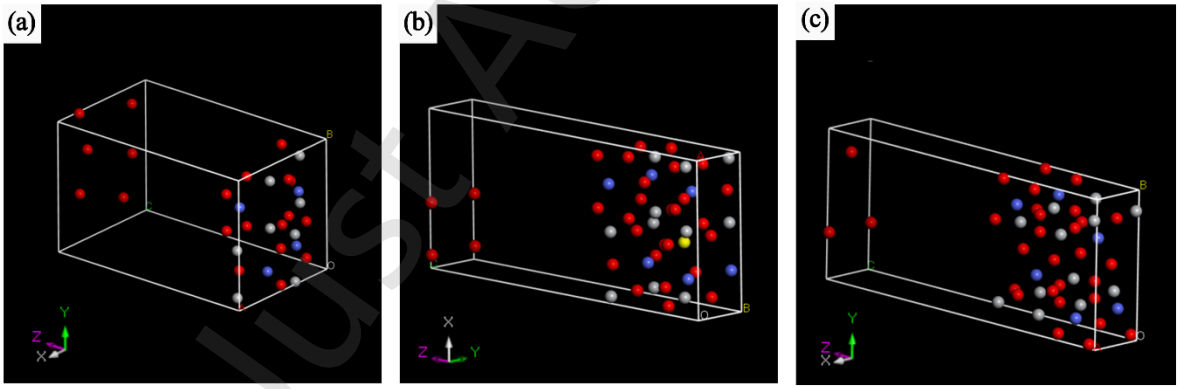

Fig. 6 The supercells created with (a) (100) plane, (b) (010) plane, and (c) (001)plane of $CoTi_2O_5$.

However, it is interesting to note that the elongated crystal planes in Fig. 5(b)-5(c) are not totally made up of the (010) and (001) planes mentioned above. AGG is also observed in additional planes with similar orientations to the (021) and (023) planes (the crystal planes are shown in purple and pink). To illustrate this phenomenon, the BFDH model is used to simulate the crystal morphology as shown in Fig. 5(e). The crystal morphology shows that the (021) and (023) planes expand along the a-axis with

the growth of the (010) and (001) planes. Therefore, it can be concluded that during the grain growth process of pseudobrookite ceramic, the (100) plane grows rapidly, causing the (010), (001), (021) and (023) planes to be elongated and eventually forming columnar crystals.

3.4 Study of the grain growth process

A formation process analysis was conducted to explain the distinctions in the grain morphology among the three MT2s. Fig. 7(a)-7(c) show the in-situ XRD patterns of the three components sintered from room temperature to 1400 ℃. It is demonstrated that high-entropy pseudobrookite ceramics are formed through a two-step solid phase process. Firstly, TiO_2 and metallic oxides react with each other to form (Mg,Co,Ni,Zn)TiO_3 ($MTiO_3$), a high-entropy intermediate phase, below 1100 ℃. As temperature rises to 1400 ℃, $MTiO_3$ and calcined TiO_2 continue to react, and finally forming high-entropy pseudobrookite ceramics. The chemical reaction equations are shown in Equation 2 and 3. As shown in Fig. 7, μ$MnTiO_3$, n$MnTiO_3$ are formed at around 1000 ℃, while μMμTiO_3, is formed at around 1100 ℃. The similar conclusion is obtained through DSC analysis, as shown in Fig. 8. In order to investigate the difference in grain morphology among these three samples during the intermediate stage of sintering, three starting material components with different grain size are sintered at 1100 ℃ for 2 h. The intermediate phases synthetized from component 1-3 are named μMμTiO_3, μ$MnTiO_3$, n$MnTiO_3$, respectively. The XRD results (Fig. 7(d)) indicate that the metallic oxides have totally disappeared after sintering at 1100 ℃ for 2 h, and all the three samples are composed of $MTiO_3$ and TiO_2-1100 ℃, with no other phases.

$$MgO + CoO + NiO + ZnO + TiO_2 \rightarrow (Mg, Co, Ni, Zn)TiO_3 \quad (2)$$

$$(Mg, Co, Ni, Zn)TiO_3 + TiO_2 \rightarrow (Mg, Co, Ni, Zn)Ti_2O_5 \quad (3)$$

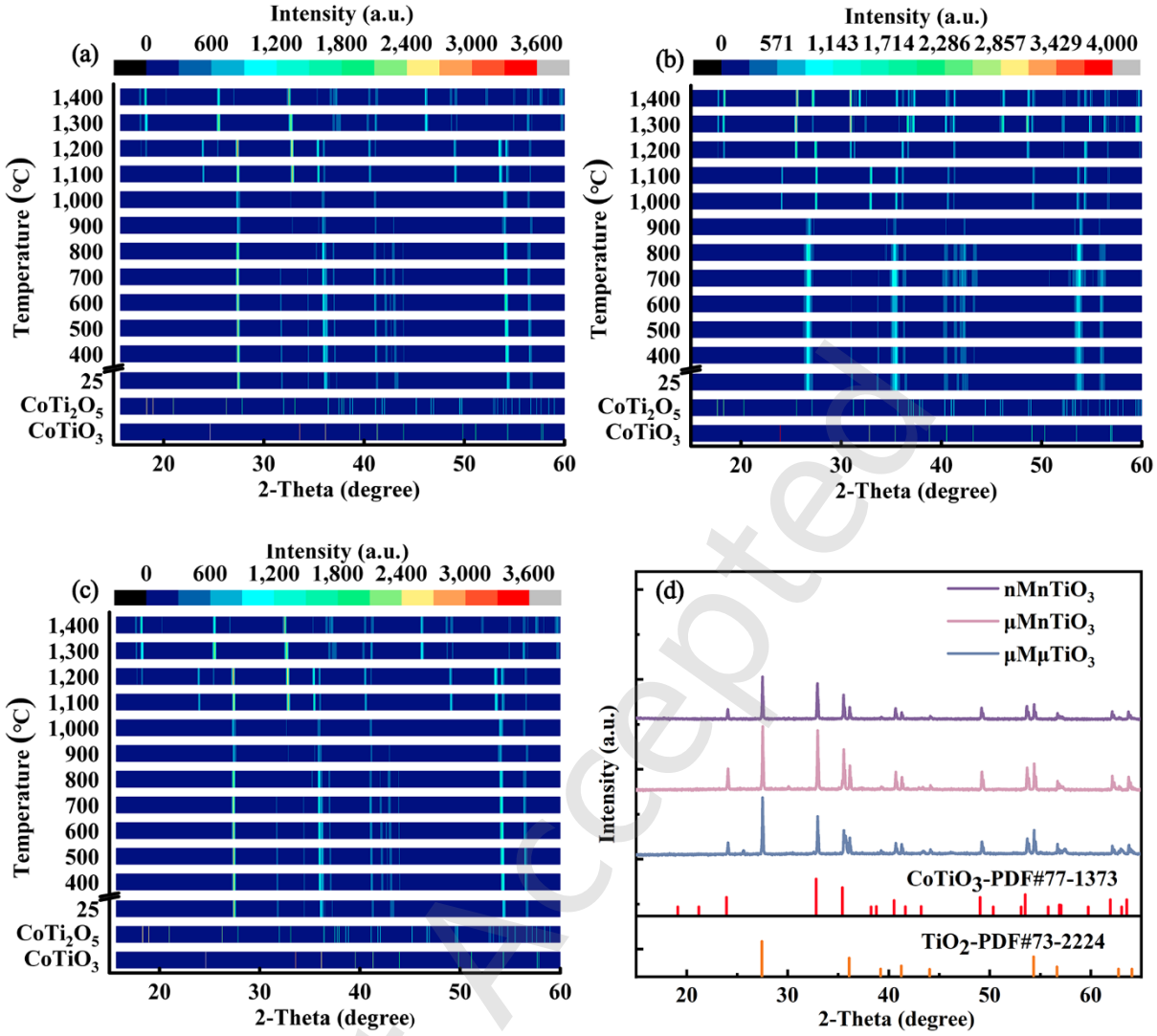

Fig. 7 In-situ XRD of (a) Component 1; (b) Component 2; (c) Component 3 after sintering from 25 ℃ to 1400 ℃; (d) XRD patterns of three components after sintering at 1100 ℃.

Fig 9 shows the backscattered electron (BSE) and EDS images of the three components sintered at 1100 ℃ for 2 h. In the BSE maps, the difference in particle brightness is caused by the difference in composition. Each of the three BSE maps shows two particles with dramatically different brightness. What's more, Mg, Co, Ni, and Zn show a significant aggregation on the brighter particles. When combined with quantitative analysis results of the elements (listed in Table 1), the lighter particles are high-entropy (Mg,Co,Ni,Zn)TiO_3, while the darker particles are TiO_2-1100 ℃.

Table 1 Quantitative analysis of the three components after sintering at 1100 ℃ (relative ratios of the molar content of each element)

		Mg	Co	Ni	Zn	Ti	O
Component 1	Specturm 1	0.05	0.037	0.046	0.047	0.190	0.630
	Specturm 2	—	—	—	—	0.324	0.676
Component 2	Specturm 1	0.038	0.033	0.042	0.045	0.220	0.622
	Specturm 2	—	—	—	—	0.335	0.665
Component 3	Specturm 1	0.035	0.029	0.034	0.042	0.214	0.646
	Specturm 2	—	—	—	—	0.349	0.651

As shown in DSC **curves** (Fig. 8), μ$MnTiO_3$ and n$MnTiO_3$ are formed before 1000 ℃, while μMμTiO_3 begins to be formed at around 1071 ℃. The formation temperature of μ$MnTiO_3$ and n$MnTiO_3$ is 100 ℃ lower than that of μMμTiO_3 which is consistent with the results of in-situ XRD patterns. It is because the sintering temperature of nano powders are lower than those of micron powders, which is driven by the small size effect and high sintering activity of nano powders [28,29]. When sintering the three components at 1100 ℃ for 2h, the densification degree of component 2 and component 3 is also slightly higher than that of component 1. The relative densities of components 2 and component 3 are 95.57% and 96.03%. However, the relative density of component 1 is 93.88%. This indicates the densification process of the three samples has been basically completed, and almost no pores are found in the three samples, as shown in Fig. 9. As the sintering temperature rises to 1400 ℃, TiO_2-1100 ℃ and $MTiO_3$ in the three samples further react with each other to form MT2. The densifications of three components are similar and all above 97%.

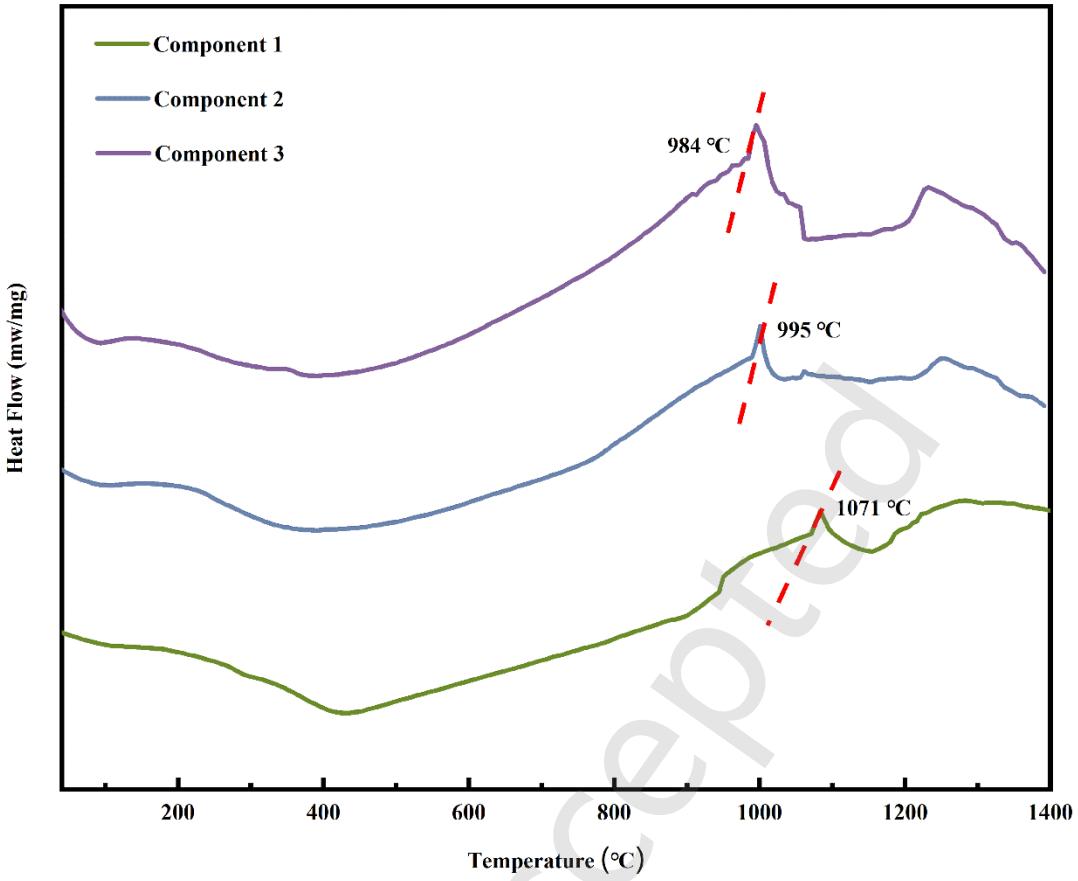

Fig. 8 DSC curves of (a) Component 1; (b) Component 2; (c) Component 3 after sintering from 25 ℃ to 1400 ℃.

As shown in Fig. 9, the average grain size of μMμTiO_3 is about 0.56 μm, while the average grain sizes of μ$MnTiO_3$ and n$MnTiO_3$ are about 1.31 μm and 1.50 μm. The diffusion barrier of nano ceramic powders is low, due to the high surface energy. It leads to nano powders diffuse rapidly as temperature rises. Therefore, the grain size of μ$MnTiO_3$ and n$MnTiO_3$ are much larger than that of μMμTiO_3. It worth noting that the average grain sizes of TiO_2-1100 ℃ in components 2 and 3 (shown in Fig. 9(b)-9(c)) are almost the same, at 2.29 μm, which is larger than those of 1.98 μm in component 1 (Fig. 9(a)). What's more, researches have shown that rutile is more likely to form elongated prism morphology with temperature increases [30]. Due to the enormous surface energy of nano-sized TiO_2, the TiO_2-1100 ℃ in components 2 and 3 have grown into rod-like shape, whereas the TiO_2-1100 ℃ in component 1 maintains its equiaxed shape. The small grain sizes of TiO_2-1100 ℃ and high-entropy

(Mg,Co,Ni,Zn)TiO_3 ensure the formed μMμT_2 has a small grain size and does not have rod-like particles which is caused by AGG, as shown in Fig. 4. Thus, it can be concluded that the grain size of the high-entropy intermediate phase and TiO_2-1100 ℃ has an important impact on the grain growth behavior of high-entropy pseudobrookite.

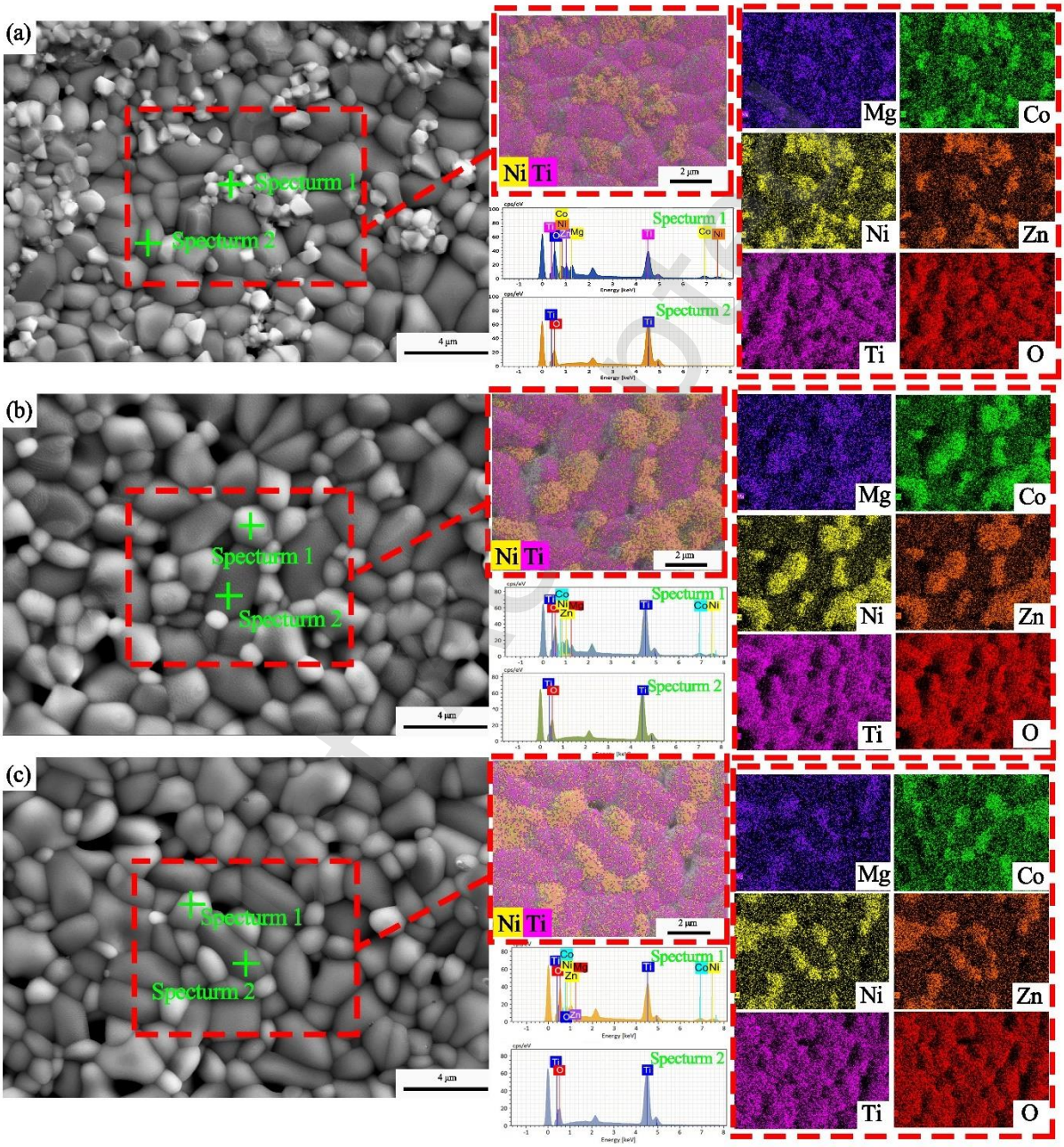

Fig. 9 SEM and corresponding EDS of (a) component 1; (b) component 2 and (c) component 3 after sintering at 1100 ℃.

3.5 Grain growth of the heat-treated ceramics

Heat treatment experiments are performed to further study the grain growth behaviors of the high-entropy (Mg,Co,Ni,Zn)Ti_2O_5 during high temperatures. The average grain size of sintered ceramics is used to study the grain development mechanism. However, there are many rod-liked grains in μMnT2 and nMnT2 due to AGG, as shown in Fig. 4. In this case, the average grain size cannot fully represent the growth of the grains. Therefore, μMμT2 is used to investigate the grain growth behaviors in this study. SEM images of μMμT2 grains after sintering at 1200-1400 ℃ for 5–15 h in air are shown in Fig. 10. It can be observed that no rod-like grains are found in all the SEM images. What's more, when sintering at 1200 ℃ and 1300 ℃, the grain growth is not particularly obvious with the prolongation of holding time. However, the grain growth of the high-entropy μMμT2 significantly faster when sintering temperature rises to 1400 ℃.

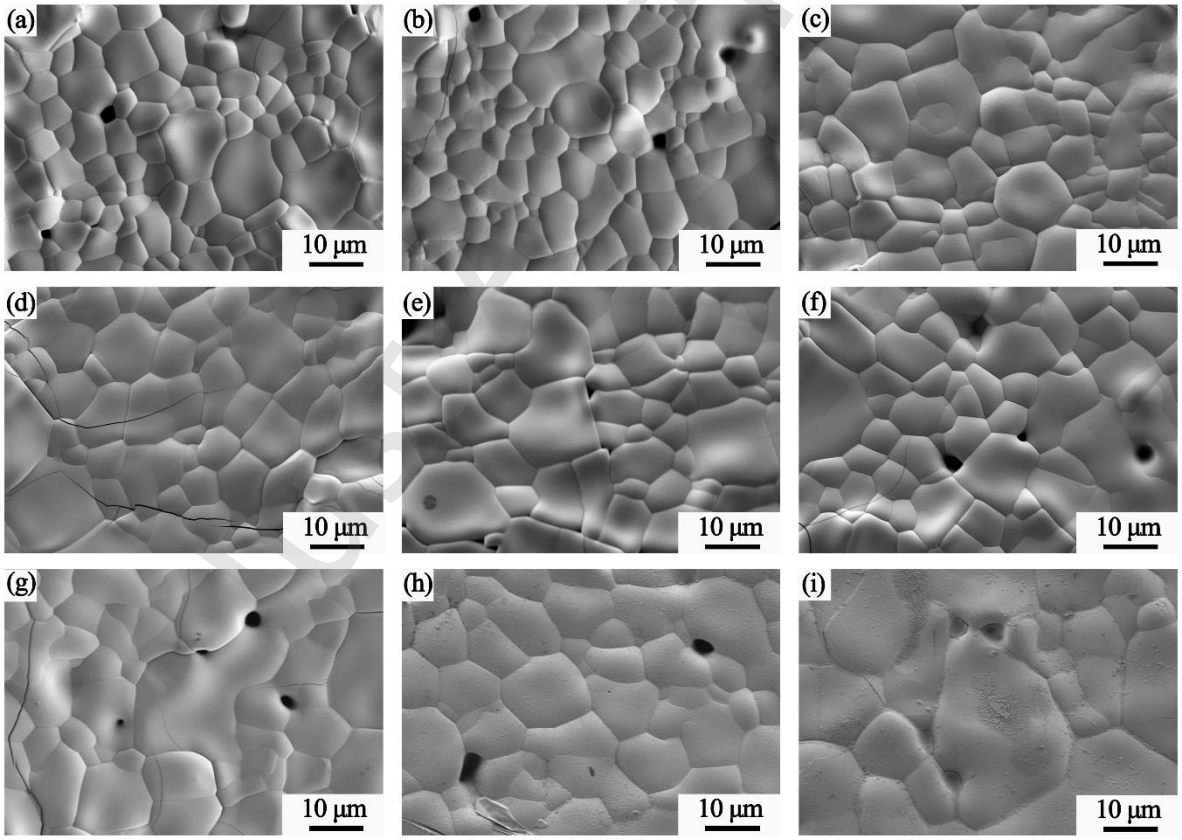

Fig. 10 Microstructure of μMμT2 after annealing at (a) 5 h, (b) 10 h, and (c) 15 h at 1200 ℃; (d) 5 h, (e) 10 h, and (f) 15 h at 1300 ℃; (g) 5 h, (h)10 h, and (i) 15 h at 1400 ℃.

Fig. 11(a) displays the statistical average grain size of 1000 μMμT2 grains after sintering at different temperatures for 5-15 h. To investigate the grain growth mechanism of the sintered ceramics during heat treatment, the average grain sizes are fitted into Eq. (4) [31]:

$$D^n - {D_0}^n = kt \quad (4)$$

where D is the average grain size at the time t; D_0 is the initial grain size, which is for the as-sintered samples without heat treatment; k is the rate constant depending on the controlling mechanism of grain growth and n is the grain growth exponent. The obtained kinetic parameters of the sintered ceramics are shown in Fig. 11(b). The n reflects different intrinsic mechanisms of grain growth and mass transfer mode, which generally ranges from 1to 4. Generally, the higher grain growth exponent indicates the stronger inhibiting influence on grain growth [32]. In this experiment, the grain growth exponent n can be determined as 3 at 1200 ℃-1400 ℃, indicating the grain growth mechanism is the surface diffusion.[31]. The above studies show that the grain growth of high-entropy pseudobrookite ceramics is a slow process, and increasing the sintering temperature is more conducive to grain growth than prolonging the holding time.

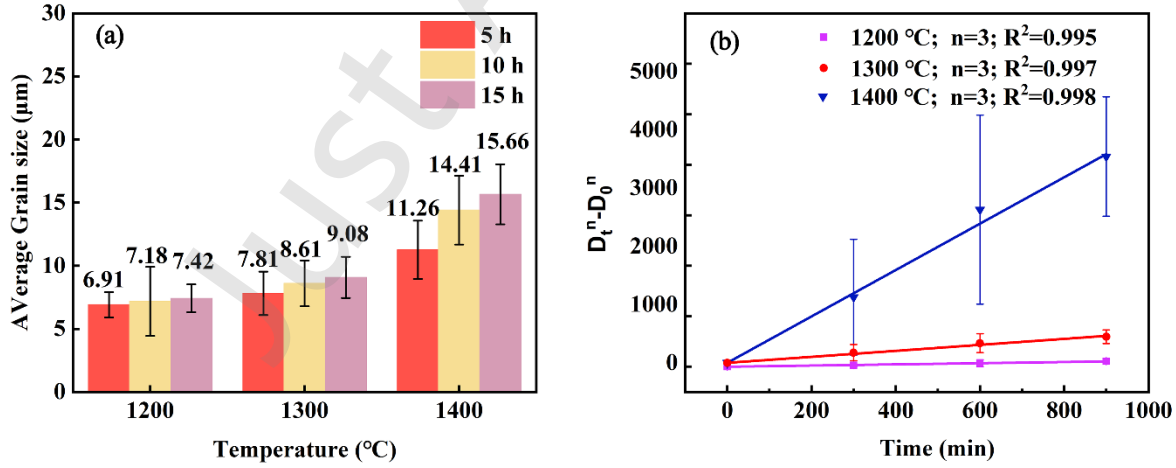

Fig. 11 (a) The average grain size and (b) Fitting kinetics parameters of the grain growth for μMμT2 at 1200 - 1400 ℃.

4 Property

The surfaces of the three MT2s are mechanically polished to a mirror finish, and the hardness and elastic modulus of the three samples are tested using nano-indentation. The force versus penetration depth (P-h) curves for determining the hardness and elastic modulus of all samples under quasi-static nanoindentation mode at a maximum load of 5 mN are shown in Fig. 12(a). During the unloading process, considerable elastic recovery can be observed, and the maximum penetration depths of the three MT2s are determined to be 126.30 nm, 148.11 nm, and 171.54 nm, respectively. The results indicate that the depth of surface penetration rises with the increase of grain size. The hardness and elastic modulus are determined by the unloading segment of the P-h curves and the results of all three MT2s are shown in Fig. 12(b). The hardness of μMμT2, μMnT2 and nMnT2 are 9.95 GPa, 7.51 GPa and 6.05 GPa, and the elastic modulus are 159.53 GPa, 137.28 GPa, and 109.08 GPa, respectively. It is well known that the strength of polycrystals always increases with grain refinement (the increase of grain boundaries number) [33]. As shown in Fig. 12(c), the average area of grain size increases with the decrease in grain sizes of starting material powders. Therefore, compared with μMnT2 and nMnT2, μMμT2 exhibits an excellent mechanical property.

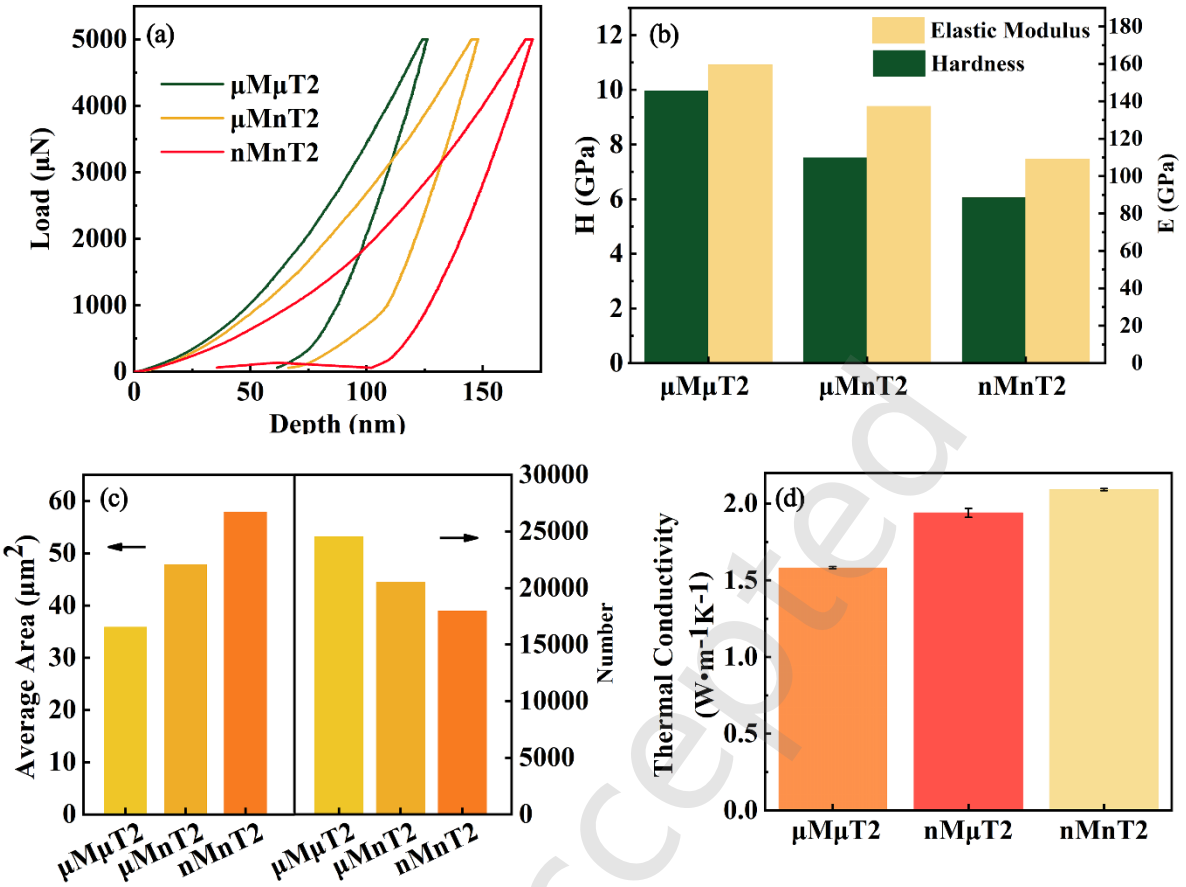

Fig.12 (a) P-h curves, (b) Hardness and Elastic module, (c) the average area of grain size vs the number of grain boundary of MT2s, (d) Thermal conductivity.

The thermal conductivity of MT2s is presented in Fig. 12(d). The thermal conductivities of μMμT2, μMnT2 and nMnT2 at room temperature are 1.583±0.006, 1.939±0.029 and 2.091±0.006 $Wm^{-1}K^{-1}$, respectively. These results demonstrate a distinct relationship between grain size and thermal diffusivity. The random arrangement of atoms or ions at grain borders leads to the dispersion and absorption of phonons while travelling through the grain boundaries [34]. These dispersion and absorption of phonons can block heat transfer, consequently reducing the material's thermal conductivity. As a result, compared with μMnT2 and nMnT2, μMμT2 exhibits a lower thermal conductivity.

5 Conclusions

In this work, high-entropy pseudobrookite ceramics were prepared using three different starting material powders with varying size distributions. It was discovered that high-entropy pseudobrookite ceramics are formed through a two-step solid phase process which differs from typical high-entropy ceramics. The in-situ XRD indicates that metallic oxides (MgO, CoO, NiO, ZnO) first react with TiO_2 to form a high-entropy intermediate phase, (Mg,Co,Ni,Zn)TiO_3. As the sintering temperature rises, high-entropy intermediate phase further react with calcined TiO_2 to form the high-entropy (Mg,Co,Ni,Zn)Ti_2O_5. The study of grain growth process indicates that besides the sluggish diffusion effect, the morphology of high-entropy intermediate phase and TiO_2-1100 ℃ are also key factors affecting grain growth in the high-entropy pseudobrookite system. The high-entropy intermediate phase and TiO_2-1100 ℃ prepared with micron-sized powders as starting materials exhibit a smaller grain size, finally resulting in the formation of high-entropy (Mg,Co,Ni,Zn)Ti_2O_5 with small grain size. According to the nano-indentation and thermal conductivity results, compared with μMnT2 and nMnT2, the μMμT2 exhibits a higher hardness of 9.95 GPa and a lower thermal conductivity of 1.583±0.006 $Wm^{-1}K^{-1}$. All these characteristics suggest that high-entropy pseudobrookite ceramics with small grain sizes have great potential in the field of high-temperature thermal protection.

Acknowledgements

The authors acknowledge the financial support from the National Natural Science Foundation of China (No. 52172072) and the National Key Research and Development Program of China (No. 2023YFB3711200).

References

[1] Rost CM, Sachet E, Borman T, *et al.* Entropy-stabilized oxides. *Nat commun,* 2015, **6**: 8485.

[2] Huimin H, Xing Y, Dai F, *et al*. High-entropy ceramics: Present status, challenges, and a look forward. *J Adv Ceram*, 2021, **10**: 385-441.

[3] Sun YN, Xiang HM, Dai FZ, *et al*. Preparation and properties of CMAS resistant bixbyite structured high-entropy oxides RE_2O_3 (RE = Sm, Eu, Er, Lu, Y, and Yb): Promising environmental barrier coating materials forAl_2O_{3f}/Al_2O_3 composites. *J Adv Ceram* 2021, **10**: 596–613.

[4] Ye YF, Wang Q, Lu J, *et al*. High-entropy alloy: challenges and prospects. *Mater Today* 2016, **19**: 349–362.

[5] Bei R, Yufeng L, Ziqian M, *et al*. Preparation and Electrical Properties Study of Non-equimolar Sr(Ti,Zr,Y,Sn,Hf)O3-σ High-entropy Perovskite Oxide. Adv Ceram 2023, 44: 342–351.

[6] Wang K, Chen L, Xu CG, *et al*. Microstructure and mechanical properties of (TiZrNbTaMo)C high-entropy ceramic. *J Mater Sci Technol* 2020, **39**: 99–105.

[7] Zhao Z, Xiang H, Dai F Z, *et al*. $(La_{0.2}Ce_{0.2}Nd_{0.2}Sm_{0.2}Eu_{0.2})_2Zr_2O_7$: A novel high-entropy ceramic with low thermal conductivity and sluggish grain growth rate. *J Mater Sci Technol* 2019, **35**: 2647-2651.

[8] Tan L, Su X, Yang J, *et al*. Facile synthesis of high-entropy zirconate nanopowders and their sintering behaviors[J]. *J Adv Ceram* 2023, **12**: 498-509.

[9] Cheng C, Zhang F, Cheng F, *et al*. The effect of plasma-assisted ball milling on preparation and sintering behavior of $(Zr_{0.1429}Hf_{0.1429}Ce_{0.1429}Y_{0.2857}La_{0.2857})$ O_2-δ high entropy fluorite oxide. *Ceram Int* 2023, **49**: 13092-13101.

[10] Zhou L, Liu J X, Tu T Z, *et al*. Fast grain growth phenomenon in high-entropy ceramics: A case study in rare-earth hexaaluminates. *J Adv Ceram* 2023, **12**: 111-121.

[11] Kornaus K, Rutkowski P, Lach R, *et al*. Effect of microstructure on thermal and mechanical properties of solid solutions Al_2TiO_5–$MgTi_2O_5$. *J Eur Ceram Soc* 2021,**41**: 1498–1505.

[12] Nakagoshi Y, Suzuki Y. Pseudobrookite-type $MgTi_2O_5$ water purification filter with controlled particle morphology. *J Asian Ceram Soc* 2015, **3**: 334–338.

[13] Suzuki Y, Shinoda Y. Magnesium dititanate ($MgTi_2O_5$) with pseudobrookite structure: A review. *Sci Technol Adv Mater* 2011, **12**: 034301.

[14] Dondi M, Lyubenova TS, Carda JB, et al. M-doped Al_2TiO_5(M = Cr, Mn, Co) solid solutions and their use as ceramic pigments. J Am Ceram Soc 2009, 92: 1972–1980.

[15] Giordano L, Viviani M, Bottino C, *et al*. Microstructure and thermal expansion of Al_2TiO_5–$MgTi_2O_5$ solid solutions obtained by reaction sintering. *J Eur Ceram Soc* 2002, **22**: 1811–1822.

[16] Wu JY, Ma XH, Hu XX, *et al*. New class of high-entropy pseudobrookite titanate with excellent thermal stability, low thermal expansion coefficient, and low thermal conductivity. *J Adv Ceram* 2022, **11**: 1654-1670.

[17] Mittal VK, Chandramohan P, Bera S, *et al*. Cation distribution in $Ni_xMg_1{-}xFe_2O_4$ studied by XPS and Mössbauer spectroscopy. *Solid State Commun* 2006, **137**: 6–10.

[18] Kim JG, Pugmire DL, Battaglia D, *et al*. Analysis of the $NiCo_2O_4$ spinel surface with Auger and X-ray photoelectron spectroscopy. *Appl Surf Sci* 2000, **165**: 70–84.

[19] Nesbitt HW, Legrand D, Bancroft GM. Interpretation of Ni2p XPS spectra of Ni conductors and Ni insulators. *Phys Chem Miner* **2000**, 27: 357–366.

[20] Sakamoto K, Hayashi F, Sato K, *et al*. XPS spectral analysis for a multiple oxide comprising NiO, TiO_2, and $NiTiO_3$. *Appl Surf Sci* 2020, **526**: 146729.

[21] Perry NH, Stevanovic V, Lim LY, *et al*. Discovery of a ternary pseudobrookite phase in the earth-abundant Ti–Zn–O system. *Dalton Trans* 2016, **45**: 1572–1581.

[22] Xiong K, Wang KZ, Chen L, *et al*. Heterostructured $ZnFe_2O_4/Fe_2TiO_5/TiO_2$ composite nanotube arrays with an improved photocatalysis degradation efficiency under simulated sunlight irradiation. *Nano-Micro Lett* 2018, **10**: 17.

[23] Zhu JT, Meng XY, Zhang P, *et al*. Dual-phase rare-earth-zirconate high-entropy ceramics with glass-like thermal conductivity. *J Eur Ceram Soc* 2021, **41**: 2861–2869.

[24] Wang F, Zhang X, Yan XL, *et al*. The effect of submicron grain size on thermal stability and

mechanical properties of high-entropy carbide ceramics. *J Am Ceram Soc* 2020, **103**:4463–4472.

[25] Giordano L, Viviani M, Bottino C, *et al*. Microstructure and thermal expansion of Al_2TiO_5–$MgTi_2O_5$ solid solutions obtained by reaction sintering. *J Eur Ceram Soc* 2002, **22**: 1811–1822.

[26] Casassa S, Pisani C. Atomic-hydrogen interaction with metalliclic lithium: An ab initio embedded-cluster study. *Phys Rev B* 1995, **51**: 7805.

[27] Polatoglou HM, Methfessel M, Scheffler M. Vacancy-formation energies at the (111) surface and in bulk Al, Cu, Ag, and Rh. *Phys Rev B* 1993, **48**: 1877.

Li WJ, Shi EW, Yin ZW. Growth habit of rutile and α-Al2O3 crystals. *J CRYST GROWTH* 2000, **208**: 546-554.

[28] Peng JH, Yi MD, Xiao GC, *et al*. Low-temperature and ultrafast dual-powder spark plasma sintering of (W, Ti) C cermets with the addition of metal core-shell nanopowder. *Int J Refract Met*, 2022, **107**: 105901.

[29] Palmeira AA., Bondioli MJ., Strecker K, *et al*. Densification and grain growth of nano-and micro-sized Y-TZP powders. *Ceram Int* 2016, **42**: 2662-2669.

[30] Akita, Atsunobu, Hisayoshi Kobayashi, Hiroaki Tada, *et al.* Action of chloride ions as a habit modifier in the hydrothermal crystal growth of rutile TiO_2 nanorod from SnO_2 seed crystal. *Chem Phys Lett* 2020, **761**: 138003.

[31] Deng SH, Yuan TC, Li RD, *et al*. Spark plasma sintering of pure tungsten powder: densification kinetics and grain growth. *Powder Technol* 2017, **310**: 264–271.

[32] Behera SK. Kinetics of grain growth in La-doped ultrapure Al_2O_3. *J. Alloy*. Compd.2016, **683**: 444–449.

[33] Han XQ, Lin N, Li AQ, *et al*. Microstructure and characterization of (Ti, V, Nb, Ta) (C, N) high-entropy ceramic. *Ceram Int* 2021, **47**: 35105-35110.

[34] Giovannelli F, Chen C, Díaz-Chao P, *et al*. Thermal conductivity and stability of Al-doped ZnO nanostructured ceramics. *J Eur Ceram Soc* 2018, **38**: 5015-5020.